

First Search for Light Dark Matter in the Neutrino Fog with XENONnT

E. Aprile ¹, J. Aalbers ², K. Abe ³, S. Ahmed Maouloud ⁴, L. Althueser ⁵, B. Andrieu ⁴, E. Angelino ^{6, 7}, D. Antón Martin ⁸, F. Arneodo ⁹, L. Baudis ¹⁰, M. Bazyk ¹¹, L. Bellagamba ¹², R. Biondi ¹³, A. Bismark ¹⁰, K. Boese ¹³, A. Brown ¹⁴, G. Bruno ¹¹, R. Budnik ¹⁵, C. Cai, ¹⁶, C. Capelli ¹⁰, J. M. R. Cardoso ¹⁷, A. P. Cimental Chávez ¹⁰, A. P. Colijn ¹⁸, J. Conrad ¹⁹, J. J. Cuenca-García ¹⁰, V. D'Andrea ^{7, *}, L. C. Daniel Garcia ⁴, M. P. Decowski ¹⁸, A. Deisting ²⁰, C. Di Donato ^{21, 7}, P. Di Gangi ¹², S. Diglio ¹¹, K. Eitel ²², S. el Morabit ¹⁸, A. Elykov ²², A. D. Ferella ^{21, 7}, C. Ferrari ⁷, H. Fischer ¹⁴, T. Flehmke ¹⁹, M. Flierman ¹⁸, W. Fulgione ^{6, 7}, C. Fuselli ¹⁸, P. Gaemers ¹⁸, R. Gaior ⁴, M. Galloway ¹⁰, F. Gao ¹⁶, S. Ghosh ²³, R. Giacomobono ²⁴, R. Glade-Beucke ¹⁴, L. Grandi ⁸, J. Grigat ¹⁴, H. Guan ²³, M. Guida ¹³, P. Gyorgy ²⁰, R. Hammann ¹³, A. Higuera ²⁵, C. Hils ²⁰, L. Hoetzsch ¹³, N. F. Hood ²⁶, M. Iacovacci ²⁴, Y. Itow ²⁷, J. Jakob ⁵, F. Joerg ^{13, 10}, Y. Kaminaga ³, M. Kara ²², P. Kavrigin ¹⁵, S. Kazama ²⁷, M. Kobayashi ²⁷, D. Koke ⁵, A. Kopec ^{26, †}, H. Landsman ¹⁵, R. F. Lang ²³, L. Levinson ¹⁵, I. Li ²⁵, S. Li ²⁸, S. Liang ²⁵, Y.-T. Lin ¹³, S. Lindemann ¹⁴, M. Lindner ¹³, K. Liu ¹⁶, M. Liu ^{1, 16}, J. Loizeau ¹¹, F. Lombardi ²⁰, J. Long ⁸, J. A. M. Lopes ^{17, †}, T. Luce ¹⁴, Y. Ma ²⁶, C. Macolino ^{21, 7}, J. Mahlstedt ¹⁹, A. Mancuso ¹², L. Manenti ⁹, F. Marignetti ²⁴, T. Marrodán Undagoitia ¹³, K. Martens ³, J. Masbou ¹¹, E. Masson ⁴, S. Mastroianni ²⁴, A. Melchiorre ^{21, 7}, J. Merz, ²⁰, M. Messina ⁷, A. Michael, ⁵, K. Miuchi ²⁹, A. Molinario ⁶, S. Moriyama ³, K. Morå ¹, Y. Mosbacher, ¹⁵, M. Murra ¹, J. Müller ¹⁴, K. Ni ²⁶, U. Oberlack ²⁰, B. Paetsch ¹⁵, Y. Pan ⁴, Q. Pellegrini ⁴, R. Peres ¹⁰, C. Peters, ²⁵, J. Pienaar ^{8, 15}, M. Pierre ¹⁸, G. Plante ¹, T. R. Pollmann ¹⁸, L. Principe ¹¹, J. Qi ²⁶, J. Qin ²⁵, D. Ramírez García ¹⁰, M. Rajado ¹⁰, R. Singh ²³, L. Sanchez ²⁵, J. M. F. dos Santos ¹⁷, I. Sarnoff ⁹, G. Sartorelli ¹², J. Schreiner, ¹³, P. Schulte ⁵, H. Schulze Eißing ⁵, M. Schumann ¹⁴, L. Scotto Lavina ⁴, M. Selvi ¹², F. Semeria ¹², P. Shagin ²⁰, S. Shi ^{1, §}, J. Shi, ¹⁶, M. Silva ¹⁷, H. Simgen ¹³, C. Szyszka, ²⁰, A. Takeda ³, P.-L. Tan ¹⁹, D. Thers ¹¹, F. Toschi ²², G. Trinchero ⁶, C. D. Tunnell ²⁵, F. Tönnies ¹⁴, K. Valerius ²², S. Vecchi ³⁰, S. Vetter ²², F. I. Villazon Solar, ²⁰, G. Volta ¹³, C. Weinheimer ⁵, M. Weiss ¹⁵, D. Wenz ⁵, C. Wittweg ¹⁰, V. H. S. Wu ²², Y. Xing ¹¹, D. Xu ¹, Z. Xu ¹, M. Yamashita ³, L. Yang ²⁶, J. Ye ³¹, L. Yuan ^{8, ¶}, G. Zavattini ³⁰ and M. Zhong ²⁶

(XENON Collaboration)**

¹ Physics Department, Columbia University, New York, NY 10027, USA

² Nikhef and the University of Groningen, Van Swinderen Institute, 9747AG Groningen, Netherlands

³ Kamioka Observatory, Institute for Cosmic Ray Research, and Kavli Institute for the Physics and Mathematics of the Universe (WPI), University of Tokyo, Higashi-Mozumi, Kamioka, Hida, Gifu 506-1205, Japan

⁴ LPNHE, Sorbonne Université, CNRS/IN2P3, 75005 Paris, France

⁵ Institut für Kernphysik, University of Münster, 48149 Münster, Germany

⁶ INAF-Astrophysical Observatory of Torino, Department of Physics, University of Torino and INFN-Torino, 10125 Torino, Italy

⁷ INFN-Laboratori Nazionali del Gran Sasso and Gran Sasso Science Institute, 67100 L'Aquila, Italy

⁸ Department of Physics, Enrico Fermi Institute & Kavli Institute for Cosmological Physics, University of Chicago, Chicago, IL 60637, USA

⁹ New York University Abu Dhabi - Center for Astro, Particle and Planetary Physics, Abu Dhabi, United Arab Emirates

¹⁰ Physik-Institut, University of Zürich, 8057 Zürich, Switzerland

¹¹ SUBATECH, IMT Atlantique, CNRS/IN2P3, Nantes Université, Nantes 44307, France

¹² Department of Physics and Astronomy, University of Bologna and INFN-Bologna, 40126 Bologna, Italy

¹³ Max-Planck-Institut für Kernphysik, 69117 Heidelberg, Germany

¹⁴ Physikalisches Institut, Universität Freiburg, 79104 Freiburg, Germany

¹⁵ Department of Particle Physics and Astrophysics, Weizmann Institute of Science, Rehovot 7610001, Israel

¹⁶ Department of Physics & Center for High Energy Physics, Tsinghua University, Beijing 100084, P.R. China

¹⁷ LIBPhys, Department of Physics, University of Coimbra, 3004-516 Coimbra, Portugal

¹⁸ Nikhef and the University of Amsterdam, Science Park, 1098XG Amsterdam, Netherlands

¹⁹ Oskar Klein Centre, Department of Physics, Stockholm University, AlbaNova, Stockholm SE-10691, Sweden

²⁰ Institut für Physik & Exzellenzcluster PRISMA+, Johannes Gutenberg-Universität Mainz, 55099 Mainz, Germany

²¹ Department of Physics and Chemistry, University of L'Aquila, 67100 L'Aquila, Italy

²² Institute for Astroparticle Physics, Karlsruhe Institute of Technology, 76021 Karlsruhe, Germany

²³ Department of Physics and Astronomy, Purdue University, West Lafayette, IN 47907, USA

²⁴ Department of Physics "Ettore Pancini", University of Napoli and INFN-Napoli, 80126 Napoli, Italy

²⁵ Department of Physics and Astronomy, Rice University, Houston, TX 77005, USA

²⁶ Department of Physics, University of California San Diego, La Jolla, CA 92093, USA

²⁷*Kobayashi-Maskawa Institute for the Origin of Particles and the Universe, and Institute for Space-Earth Environmental Research, Nagoya University, Furo-cho, Chikusa-ku, Nagoya, Aichi 464-8602, Japan*

²⁸*Department of Physics, School of Science, Westlake University, Hangzhou 310030, P.R. China*

²⁹*Department of Physics, Kobe University, Kobe, Hyogo 657-8501, Japan*

³⁰*INFN-Ferrara and Dip. di Fisica e Scienze della Terra, Università di Ferrara, 44122 Ferrara, Italy*

³¹*School of Science and Engineering, The Chinese University of Hong Kong, Shenzhen, Guangdong, 518172, P.R. China*
(Dated: September 27, 2024)

We search for dark matter (DM) with a mass [3, 12] GeV/c^2 using an exposure of $3.51 \text{ t} \times \text{y}$ with the XENONnT experiment. We consider spin-independent, spin-dependent, momentum-dependent, mirror DM, and self-interacting DM with a light mediator coupling to Standard Model particles. Using a lowered energy threshold compared to the previous WIMP search, a blind analysis of [0.5, 5.0] keV nuclear recoil events reveals no significant signal excess over the background. XENONnT excludes spin-independent DM-nucleon cross sections $> 2.5 \times 10^{-45} \text{ cm}^2$ at 90% confidence level for 6 GeV/c^2 DM. The solar ^8B neutrino coherent elastic neutrino-nucleus scattering background accounts for approximately half of the background in the signal region. In the considered mass range, the DM sensitivity approaches the ‘neutrino fog’, the limitation where neutrinos produce a signal that is indistinguishable from that of light DM-xenon nucleus scattering.

Introduction — The XENONnT experiment [1], operated at INFN Laboratori Nazionali del Gran Sasso, is primarily designed to search for weakly interacting massive particles (WIMPs) [2–4] with a mass scale of GeV/c^2 – TeV/c^2 . By lowering the energy threshold compared to our previous WIMP search [5], we are able to improve the sensitivity to light dark matter (DM). However, as we increase the exposure, the solar ^8B neutrino coherent elastic neutrino-nucleus scattering (CE ν NS) background begins to affect the sensitivity gain. This gradual slowdown in sensitivity improvement for light DM with additional exposure is known as neutrino fog [6–10]. In this Letter, we report on the first search for light DM with a mass [3, 12] GeV/c^2 , achieving DM sensitivities into the neutrino fog. This search utilizes the same dataset and analysis techniques as in our recently reported search for solar ^8B neutrino via CE ν NS interaction [11].

The XENONnT experiment comprises a central detector, operating as a time projection chamber (TPC), with an active target of 5.9 tonnes of cryogenic liquid xenon, enclosed by a Cherenkov neutron veto (NV) and muon veto [12] detector to mitigate radiogenic neutrons and cosmogenic muon-induced backgrounds. The operation of XENONnT is supported by various subsystems, including a gas-phase and a liquid-phase xenon circulation and purification system, a radon removal system [13], and a krypton distillation column [14]. A particle interaction in the xenon target may produce a nuclear recoil (NR) with the xenon nucleus, or an electronic recoil (ER) with the atomic electrons. Two arrays of photomultiplier tubes (PMTs) at the top and bottom of the TPC collect the light from the scintillation signal (S1) and ionization signal (S2), converting them to photo-electrons (PE). The digitizer converts the PE waveforms that cross the digitization thresholds into PMT hits, which are clustered into peaks by reconstruction software [15, 16]. The detector wall consists of Polytetrafluoroethylene (PTFE) panels to enhance photon gain (g1). A cathode near the bottom of the TPC and gate electrodes below the liquid-

gas interface generate a vertical electric field of approximately 23 V/cm, which drifts the ionization electrons to the liquid-gas interface with a maximum drift time of 2.2 ms. An extraction field is generated by the gate and anode electrodes, leading to the secondary scintillation of the extracted electrons. The extraction efficiency and single electron scintillation gain contribute to the electron gain (g2). Further details on XENONnT can be found in Ref. [1].

Dataset — This DM search combines data from two Science Runs spanning from May 1, 2021, to December 10, 2021 (SR0, livetime 108.0 days), and from May 19, 2022, to August 8, 2023 (SR1, livetime 208.5 days). Between SR0 and SR1, the radon distillation system was upgraded to operate in both gas xenon (GXe) and liquid xenon (LXe) modes. On July 15, 2022, the liquid level was decreased by 0.2 mm from (5.0 ± 0.2) mm and the anode voltage was increased from 4.90 kV to 4.95 kV to mitigate clustered electron emissions, while keeping a constant electron gain. In SR0 (SR1), the average electron lifetime is 14.2 ms (20.1 ms), g1 is $0.1515 \pm 0.0014 \text{ PE/photon}$ ($0.1367 \pm 0.0010 \text{ PE/photon}$), and g2 is $16.45 \pm 0.64 \text{ PE/e}^-$ ($16.85 \pm 0.46 \text{ PE/e}^-$).

Signal — We consider a DM with mass ranging from 3 to 12 GeV/c^2 , a mass range favored by light DM models such as asymmetric and self-interacting DM [17–22]. We examine five DM models involving nuclear recoils from elastic scattering of DM on the xenon nuclei: spin-independent (SI) [23], spin-dependent (SD) [24], self-interacting DM with a light mediator (SI-LM) [20], momentum-dependent DM scattering (MDDM) [25], and mirror DM [26]. The spectrum of SI DM is evaluated using Ref. [27] and is visualized in Fig. 1 (top). For astrophysical models and nuclear form factors, we follow Ref. [5] with the exception of mirror DM, where we adopt DM-mass-dependent Boltzmann velocity v_0 as assumed in Ref. [28].

The average number of scintillation photons and ionization electrons from the energy of an NR interaction

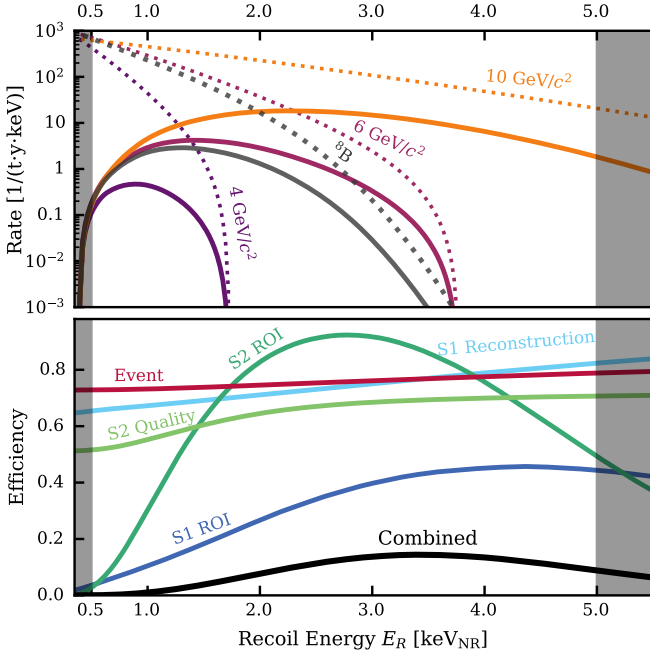


FIG. 1. Top: The SI DM signal spectrum with a cross section of 4.4×10^{-45} cm² before (dotted) and after (solid) accounting for the signal efficiency. The ⁸B CE ν NS spectrum (gray) is shown for comparison. Bottom: The signal efficiency (black) is a combination of individual efficiencies of S1 ROI (blue), S1 reconstruction (light blue), S2 ROI (dark green), S2 quality selection (light green), and event efficiency (red). These efficiencies are evaluated per science run and weighted by livetime.

(E_R) is quantified by the light yield model L_y and the charge yield model Q_y . We model detector responses for low-energy NR events [29] with ⁸⁸YBe neutron calibration data [30] (with a mean $\bar{E}_R \approx 2$ keV per scatter), and fit L_y and Q_y following the methodology described in Ref. [31]. Yields for $E_R < 0.5$ keV are assumed to be zero, and light DM signals with $E_R > 5.0$ keV are neglected. For $E_R < 5.0$ keV, the ⁸⁸YBe calibrated yield model aligns with the Q_y of the NEST v2.3.6 [32] yield model within systematic uncertainty, while the L_y uncertainties generally encompass the median of the NEST model. The uncertainties of L_y and Q_y are modeled using shape parameters, denoted as t_{Ly} and t_{Qy} , respectively, which parametrize the uncertainty bands.

A simulation-based detector response model converts the produced photons and electrons to detector observables [33]. Using the depth (Z) and radius (R) position of the event, the fiducial volume (FV) is defined as $-142.0 \text{ cm} \leq Z \leq -13.0 \text{ cm}$, $R \leq 60.2 \text{ cm}$ for SR0 and $R \leq 59.6 \text{ cm}$ for SR1. The region of interest (ROI) is defined as 2 or 3 hits for S1 and [120, 500] PE, corresponding to approximately [4, 16] extracted electrons for S2. Events reconstructed with $R \leq 63.0 \text{ cm}$ in the ROI were blinded before finalizing the analysis. Compared to

the previous XENONnT NR search [5], the ROI in this Letter leads to a 17 times higher signal rate expectation for a 6 GeV/c² SI DM. The overlap of ROI between this Letter and the previously unblinded SR0 WIMP search [5] was reblinded and used in this search.

Three types of selection are implemented, following the ⁸B CE ν NS analysis [11]. For the S1 peaks, the reconstruction requires a two-fold PMT coincidence. For the S2 peaks, other than the waveform width and PMT distribution quality selections inherited from Ref. [5], an S2 boosted-decision-tree machine is developed as detailed in the background section. To mitigate unphysical events resulting from detector artifacts, we implement selections that consider temporal and spatial correlations with preceding high-energy (HE) events [11], including $S2_{\text{pre}}/\Delta t_{\text{pre}}$, defined as the ratio between the S2 peak area of HE events and the time difference from candidate events. Following Ref. [5], a single-scatter selection is applied. A selection based on the single electron (SE) rate within a preceding 5-second time window is implemented to mitigate the impact of localized SE bursts.

The signal efficiency is derived by combining the ROI efficiency, the S1 reconstruction efficiency, the S2 quality selection efficiency, and the event efficiency, as illustrated in Fig. 1 (bottom). Excluding yield model uncertainties, the systematic uncertainty of the combined efficiency is estimated to be 25%, predominantly due to the uncertainties in the S1 reconstruction efficiency and the S2 quality selection efficiency.

The ROI efficiency is assessed through detector reconstruction simulation and is sensitive to the yield model. For a 6 GeV/c² SI DM, the signal efficiency uncertainty due to the yield model alone is estimated to be 34%, resulting from the propagation of uncertainties in t_{Ly} and t_{Qy} to the signal rate computation.

The S1 reconstruction efficiency originates from the two-fold S1 coincidence requirement. We employ a data-driven method [33] that simulates low energy S1 waveforms by sampling a subset of photon waveforms from ^{83m}Kr 32.1 keV and 9.4 keV conversion electrons and ³⁷Ar 2.8 keV electron capture calibration data. We incorporate a conservative systematic uncertainty of 10% to account for the systematic uncertainty in the shape of the S1 waveform. The S1 reconstruction efficiency is 65% (85%) for S1 signals with 2 (3) detected photons, while the other S1 quality selections achieve acceptances over 99% and are thus neglected in efficiency evaluation.

The S2 quality selection efficiency is evaluated by studying the selection survival ratio of evaluation datasets within the ROI, including waveform simulation [35], surface ²¹⁰Pb β events from PTFE, ²¹⁴Pb β events from the cathode, ³⁷Ar 0.27 keV electron capture, and NV-tagged low energy ²⁴¹AmBe neutrons. A systematic uncertainty of 10% is adopted based on the variation among the evaluation datasets.

The event reconstruction algorithm pairs one S1 to one

TABLE I. For each model component, we show the background expectation and best-fit values for the background-only hypothesis, background and SI DM signal hypothesis with a 4, 6, 10 GeV/c^2 mass DM. The expectation uncertainties for ${}^8\text{B}$ CE ν NS background consider both signal efficiency uncertainty and yield uncertainties while neglecting the subdominant 3% ${}^8\text{B}$ neutrino flux uncertainty [34]. Other uncertainties are calculated using the profile likelihood method. In addition to the event number in the full ROI, the event number in the most signal-like region is shown in parentheses, which is defined to contain 50% of the signal for bins ranked by signal-to-background ratio. The best-fit and nominal values agree within the uncertainties for all components.

Component	Expectation	Background-only	4 GeV/c^2	6 GeV/c^2	10 GeV/c^2
SI DM	—	—	3.2 (1.6)	0.0 (0.0)	0.0 (0.0)
${}^8\text{B}$ CE ν NS	$11.9^{+4.5}_{-4.2}$	$11.4^{+2.0}_{-3.6}$	10.2 ± 2.7 (2.5 ± 0.7)	$11.4^{+2.7}_{-2.6}$ (6.0 ± 1.4)	$11.4^{+2.7}_{-2.6}$ ($5.4^{+1.3}_{-1.2}$)
AC	25.3 ± 1.2	$25.3^{+1.1}_{-1.3}$	25.1 ± 1.2 (3.7 ± 0.1)	25.3 ± 1.2 (4.1 ± 0.2)	25.3 ± 1.2 (3.3 ± 0.1)
ER	0.7 ± 0.7	$0.5^{+0.7}_{-0.6}$	$0.6^{+0.7}_{-0.6}$ (0.0 ± 0.0)	$0.5^{+0.6}_{-0.5}$ (0.3 ± 0.3)	$0.5^{+0.7}_{-0.5}$ ($0.4^{+0.5}_{-0.4}$)
Neutron	$0.5^{+0.2}_{-0.3}$	0.5 ± 0.3	0.5 ± 0.3 (0.1 ± 0.1)	0.5 ± 0.3 (0.2 ± 0.1)	0.5 ± 0.3 (0.2 ± 0.1)
Total background	$38.3^{+4.7}_{-4.4}$	$37.7^{+2.5}_{-3.9}$	$36.4^{+3.0}_{-3.0}$ ($6.3^{+0.7}_{-0.7}$)	$37.7^{+3.0}_{-2.9}$ ($10.6^{+1.5}_{-1.4}$)	$37.7^{+3.0}_{-2.9}$ ($9.2^{+1.4}_{-1.3}$)
Observed	—	37	37 (10)	37 (10)	37 (4)

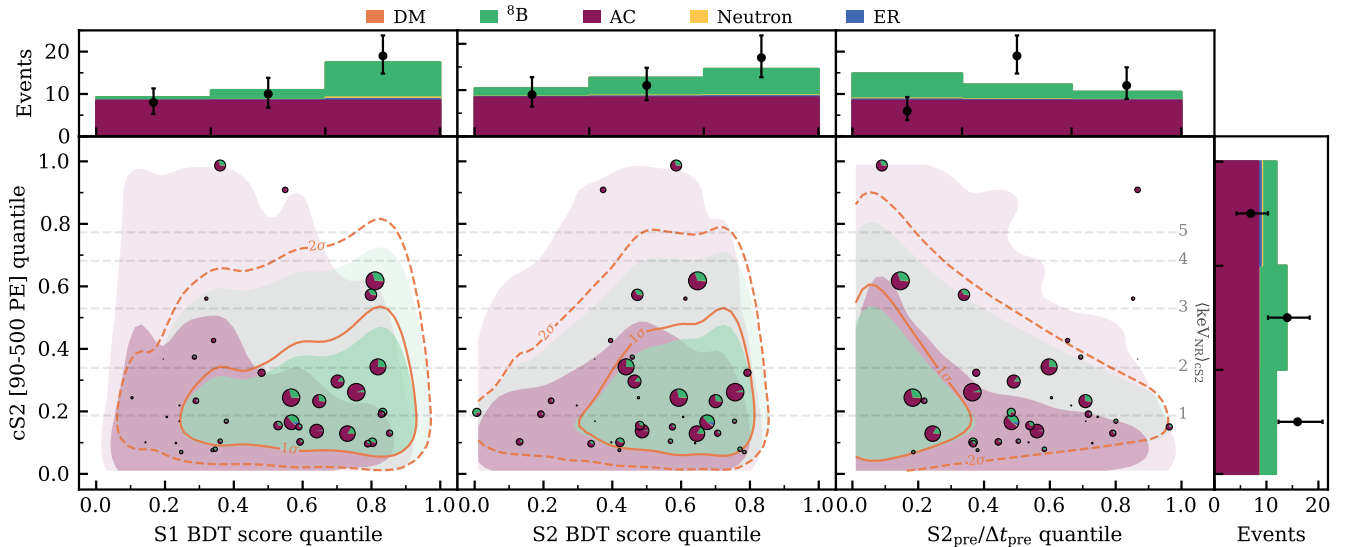


FIG. 2. DM candidate events in the search space, distributed in quantiles of (S1 BDT, cS2) (left), (S2 BDT, cS2) (center) and (S2_{pre}/Δt_{pre}, cS2) (right). Events after selections are shown as pie charts, with each wedge representing the contribution of the components in the best-fit model assuming a 6 GeV/c^2 DM. The size of the pie charts is proportional to the absolute DM best-fit rate. The contributions of DM, ER, and neutron events in the wedges and histograms are not visible since the best-fit rates are negligible. The shaded contours show the 1σ and 2σ distributions of the AC background (purple) and solar ${}^8\text{B}$ CE ν NS background (green). The solid and dashed line contours show the 1σ and 2σ distribution of a 6 GeV/c^2 DM signal (orange), showing its similarity with ${}^8\text{B}$ CE ν NS. The equivalent nuclear recoil energy based solely on cS2 is indicated by the gray lines. The one-dimensional projection of best-fit and observed data (black) is shown on the side.

S2 peak to build an event. The algorithm may fail when S1 and S2 peaks, of areas similar to candidate events, occur within a time window of $\mathcal{O}(10)$ ms. To account for this effect, along with the aforementioned event selections, the event efficiency is evaluated per science run by tracking the survival ratio of simulated events randomly inserted into real data. The event efficiency is 77% (73%) for 2-hit S1, and 82% (78%) for 3-hit S1 in SR0 (SR1) within the ROI.

Backgrounds — This analysis considers the background described in Refs. [5, 31, 36]. The expected rate

and systematic uncertainties, both in the ROI and in the signal-like region, are summarized in Table I.

The solar ${}^8\text{B}$ CE ν NS interaction, whose recoil spectrum is nearly indistinguishable from a 5.5 GeV/c^2 DM-nucleon scattering at cross-section $4.4 \times 10^{-45} \text{ cm}^2$, is one of the dominant backgrounds of this search. Following the recommended convention [37], the predicted solar ${}^8\text{B}$ CE ν NS event rate is (3.6 ± 0.9) events $\text{t}^{-1} \text{y}^{-1}$ in SR0 and (3.3 ± 0.8) events $\text{t}^{-1} \text{y}^{-1}$ in SR1, based on the standard solar model ${}^8\text{B}$ neutrino spectrum [38] and the measured flux of $(5.25 \pm 0.20) \times 10^6 \text{ cm}^{-2} \text{s}^{-1}$ from

SNO [34], using the nominal NR yield model.

The accidental coincidence (AC) background arises from the accidental pairing of isolated S1 and isolated S2 peaks, where ‘isolated’ refers to peaks that lack a physically corresponding S1 or S2 [11, 39]. The quality selections outlined in the signal section reduce the isolated S1 and S2 peak rates to 2.3 (2.2) Hz for S1 and 18 (26) mHz for S2 in SR0 (SR1). Utilizing a synthesized data-driven AC dataset [31, 36], two boosted decision tree (BDT) classifiers, S1 BDT and S2 BDT, are trained on an equivalent $6 \text{ GeV}/c^2$ DM signal, each targeting AC of different origins. The S1 BDT distinguishes isolated S1 signals originating from random PMT hit clustering by incorporating S1 hit counts, PMT channel distribution, double photo-electron emission [40], and S1 pulse shape [41] into the S1 BDT score. The S2 BDT evaluates whether the S2 pulse shape of the candidate event is compatible with the expectation of electron diffusion [42], converting this assessment into an S2 BDT score. These waveform-feature-based BDT scores are used as an inference dimension to enhance signal-to-background discrimination power, as shown in Fig. 2. An AC sideband, primarily consisting of events rejected by the S2 BDT selection, was unblinded before the ROI unblinding to examine the validity of the AC modeling. Subsequently, the S2 area threshold of the ROI was raised from 100 PE to 120 PE due to an observed tension between the observation and the AC background model. The discrepancy in the AC rate between the unblinding result of the AC sideband and the prediction is then less than 5%, and the statistical uncertainty of the AC sideband data is conservatively chosen to be the systematic uncertainty of the AC background. The details of sideband validation can be found in Ref. [11]. The AC background prediction is (6.4 ± 0.6) events $\text{t}^{-1} \text{y}^{-1}$ in SR0 and (7.6 ± 0.4) events $\text{t}^{-1} \text{y}^{-1}$ in SR1.

The surface background originates from ^{222}Rn progeny plate-out on the PTFE panels, such as β decays from ^{210}Pb ($\bar{E}_R \approx 6.1 \text{ keV}_{\text{ER}}$). This can result in a higher background rate in the ROI due to the presence of S2 charge-insensitive volumes and the worse position reconstruction resolution of small S2 signals ($\Delta R \approx 2 \text{ cm}$) near the detector wall. The surface background is modeled in a data-driven manner using non-blinded events. The FV is selected to mitigate the surface background contribution, yielding a negligible rate of less than 0.10 events $\text{t}^{-1} \text{y}^{-1}$ at 90% CL. The prediction is validated by a sideband unblinding of events within $61.4 \text{ cm} < R < 63.0 \text{ cm}$. Due to the negligible rate, the surface background is not included in the statistical model.

The radiogenic neutron background originates from nuclear fission and the (α, n) process in the uranium and thorium decay chains. It is modeled using full-chain simulations as described in Ref. [31]. The levels of radioactive contamination, as determined from

the radioassay [5], are further adjusted based on the comparison between observed and simulated high energy γ ray activity. The prediction of the neutron background is (0.11 ± 0.06) events $\text{t}^{-1} \text{y}^{-1}$ in SR0 and (0.14 ± 0.08) events $\text{t}^{-1} \text{y}^{-1}$ in SR1, considering an effective neutron veto tagging efficiency of 49% (SR0) and 52% (SR1).

The electronic recoil (ER) background originates from internal radioactive contaminations, including the β decays of ^{214}Pb , ^{85}Kr , material γ rays, and the neutrino-electron weak interaction of the solar pp neutrinos [43]. The ER rates per SR are determined by fitting the already unblinded events in the $[1, 140]$ keV range in SR0 [43] and the non-blinded events in the $[10, 140]$ range keV in SR1. Due to the uncertainty of the shape of the ER background energy spectrum, a systematic uncertainty of 100% is assigned to the ER background, under the assumption of a flat ER energy spectrum in the ROI and utilizing the combined fit yield model from SR0 ^{220}Rn and ^{37}Ar calibration data [31]. The conservative uncertainty has minimal impact on our results due to the low rate of ER background. The prediction of ER background is (0.11 ± 0.11) events $\text{t}^{-1} \text{y}^{-1}$ in SR0 and (0.24 ± 0.24) events $\text{t}^{-1} \text{y}^{-1}$ in SR1, and the difference between SRs is due to an increased concentration of ^{85}Kr at the start of SR1 which was subsequently removed by cryogenic distillation.

Inference — An extended binned likelihood function is constructed for the SR0 and SR1 data using four analysis dimensions: corrected S2 (cS2), S1 BDT score, S2 BDT score, and $S2_{\text{pre}}/\Delta t_{\text{pre}}$. The bin edges are defined by binning the AC background in each dimension with equal probability, as shown in Fig. 2, resulting in a total of $3^4 = 81$ bins in the 4D histogram. The likelihood function is expressed as:

$$\mathcal{L}(\sigma, \boldsymbol{\theta}) = \mathcal{L}_{\text{SR0}}(\sigma, \boldsymbol{\theta}) \cdot \mathcal{L}_{\text{SR1}}(\sigma, \boldsymbol{\theta}) \cdot \prod_m \mathcal{L}_m^{\text{anc}}(\theta_m), \quad (1)$$

where σ represents the DM-nucleon interaction cross section, and $\boldsymbol{\theta}$ are the Gaussian ancillary likelihood-constrained nuisance parameters. The index m iterates through the nuisance parameters, including the expected rate of each background with their uncertainties shown in Table. I, the signal efficiency with 25% uncertainty, and the NR yield model shape parameters ($t_{\text{Ly}}, t_{\text{Qy}}$).

Prior to unblinding, the sensitivity band was determined by computing the profile-log-likelihood-ratio test statistics between the signal-plus-background hypothesis and the background-only hypothesis using toy Monte-Carlo datasets [37, 52, 53]. We adopt a power-constrained limit (PCL) [54] with a power threshold of -1σ to report the final limit. The power threshold is changed from our previous 50% threshold [5] to be in line with the limits reported by other experiments. A future publication will discuss the difference between PCL thresholds and further motivate this choice.

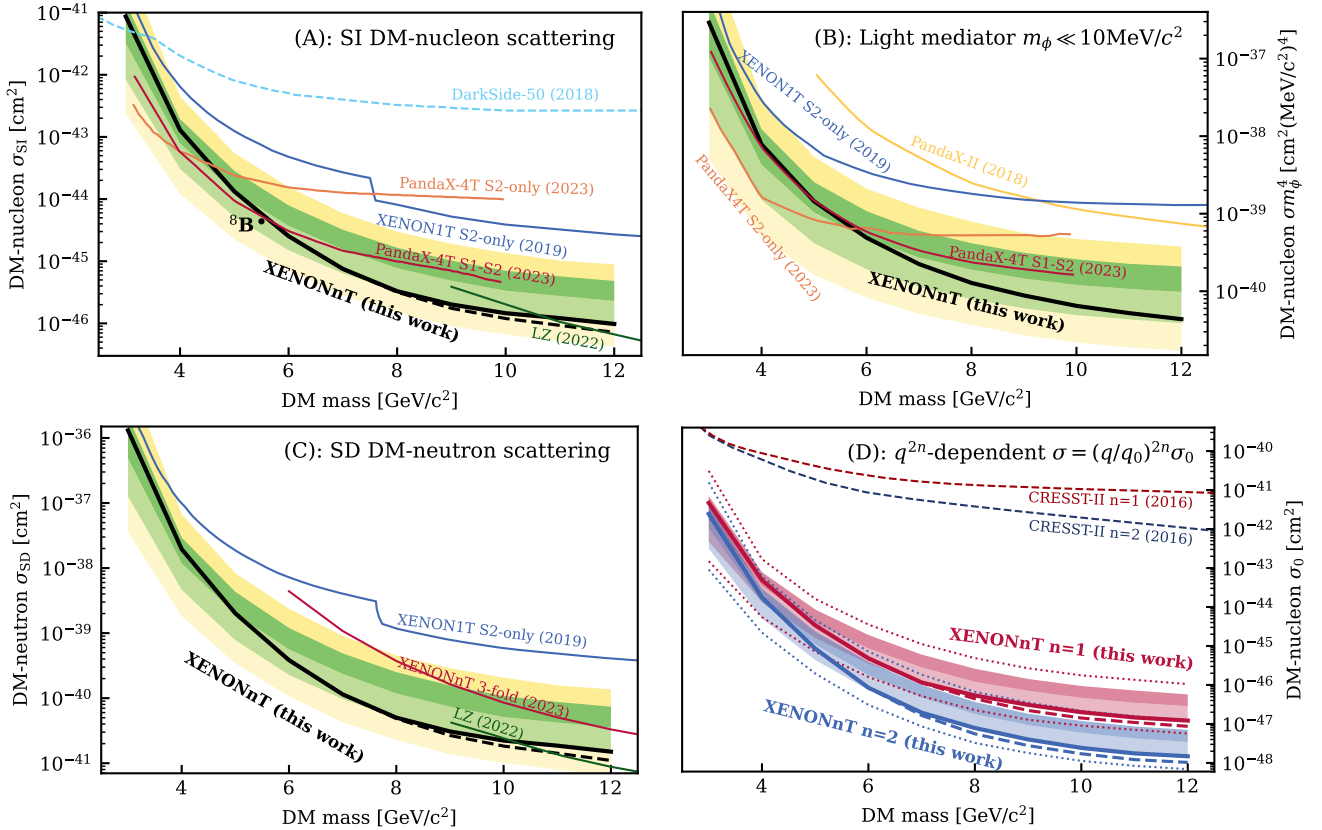


FIG. 3. DM cross section upper limit at 90% confidence level with the 1σ (green) and 2σ (yellow) sensitivity band. The results with and without sensitivity -1σ PCL are shown by solid and dashed lines, respectively. Previous results are shown for comparison [44–49], where limits from other liquid-xenon-based experiments are power-constrained to sensitivity -1σ . (A) shows the constraint on SI DM-nucleon interaction. The neutrino fog [6] is defined as $n = \max_{\sigma \in [\sigma_0, \infty]} \left[-\left(\frac{d \ln \sigma}{d \ln M T} \right)^{-1} \right]$, in which $n=2, 2.5, 3$ from lighter to darker gray. The ${}^8\text{B}$ CE ν NS equivalent DM of $5.5 \text{ GeV}/c^2$ with cross section $4.4 \times 10^{-45} \text{ cm}^2$ is shown. (B) shows the constraints on SI-LM, the differential rate is proportional to σm_ϕ^4 assuming $m_\phi \ll q \approx 10 \text{ MeV}$ [44, 50], where m_ϕ is the mediator mass, and q is the momentum transfer. (C) shows the constraint on SD DM-neutron interaction assuming the median of nuclear form factors from Ref. [51]. (D) shows the constraint on MDDM assuming a cross section of the form $\sigma_{\chi N} = (q/q_0)^{2n} \sigma_0$ with momentum dependence $n = 1, 2$ (red, blue), where σ_0 is the SI cross section, and q_0 is a normalization factor chosen to be $10 \text{ MeV}/c$ [48]. The 2σ sensitivity bands are depicted using dots.

Results — After unblinding, SR0 and SR1 reveal 9 and 28 events, respectively. The discovery p-value for the DM of SI interaction indicates no significant excess, with a minimum p-value of 0.18 at $3 \text{ GeV}/c^2$. Their distributions in the search space are shown in Fig. 2. The background-only and signal-plus-background best-fits for $4, 6, 10 \text{ GeV}/c^2$ DMs are presented in Table I. Two goodness-of-fit (GOF) tests, with a reporting p-value threshold of 0.025 determined prior to unblinding, are performed on the spatial X - Y dimension. The resulting p-values, 0.018 and 0.037, suggest potential spatial clustering of events. However, the positions are not used in the inference framework defined prior to unblinding. Post-unblinding checks including inspection of the distribution in data selection space as well as the event waveforms show no indication of mismodeling.

The results for SI, SD, MDDM, and SI-LM, along with

previous limits [44–49], are presented in Fig. 3 for comparison. Our results tighten the constraints across the parameter spaces for all listed DM models, with the SI limit at the benchmark $6 \text{ GeV}/c^2$ DM mass reaching $2.5 \times 10^{-45} \text{ cm}^2$. An upward fluctuation is observed below $5 \text{ GeV}/c^2$ and a downward fluctuation above this mass. The SD DM-neutron limit is susceptible to the current $\sim 10\%$ uncertainty of the nuclear form factors in Ref. [51]. As the uncertainty predominately changes the expected recoil rate, the results presented here can be rescaled. Additionally, we exclude all metallic components of mirror DM proposed by Ref. [26, 28], specifically ruling out mirror oxygen with a 90% upper limit on the rate parameter $\epsilon\sqrt{\xi_{O'}}$ of 1.3×10^{-12} , with the theoretically favored region $10^{-11} \lesssim \epsilon\sqrt{\xi_{O'}} \lesssim 4 \times 10^{-10}$.

XENONnT achieves the world-leading sensitivity for light DM candidates within the ${}^8\text{B}$ CE ν NS neutrino fog,

as illustrated by Fig. 3 (A). The background-only model yields a best-fit of $11.4^{+2.0}_{-3.6}$ ^8B CE ν NS events. In the 6 GeV/c^2 model, ^8B CE ν NS emerges as the most significant background, accounting for 60% of the total background in the signal-like region, marking the first step into the neutrino fog.

Acknowledgements — We gratefully acknowledge support from the National Science Foundation, Swiss National Science Foundation, German Ministry for Education and Research, Max Planck Gesellschaft, Deutsche Forschungsgemeinschaft, Helmholtz Association, Dutch Research Council (NWO), Fundacao para a Ciencia e Tecnologia, Weizmann Institute of Science, Binational Science Foundation, Région des Pays de la Loire, Knut and Alice Wallenberg Foundation, Kavli Foundation, JSPS Kakenhi, JST FOREST Program, and ERAN in Japan, Tsinghua University Initiative Scientific Research Program, DIM-ACAV+ Région Ile-de-France, and Istituto Nazionale di Fisica Nucleare. This project has received funding/support from the European Union’s Horizon 2020 research and innovation program under the Marie Skłodowska-Curie grant agreement No 860881-HIDDeN.

We gratefully acknowledge support for providing computing and data-processing resources of the Open Science Pool and the European Grid Initiative, at the following computing centers: the CNRS/IN2P3 (Lyon - France), the Dutch national e-infrastructure with the support of SURF Cooperative, the Nikhef Data-Processing Facility (Amsterdam - Netherlands), the INFN-CNAF (Bologna - Italy), the San Diego Supercomputer Center (San Diego - USA) and the Enrico Fermi Institute (Chicago - USA). We acknowledge the support of the Research Computing Center (RCC) at The University of Chicago for providing computing resources for data analysis.

We thank the INFN Laboratori Nazionali del Gran Sasso for hosting and supporting the XENON project.

[arXiv:hep-ph/9506380](https://arxiv.org/abs/hep-ph/9506380).

- [4] G. Bertone and D. Hooper, History of dark matter, *Rev. Mod. Phys.* **90**, 045002 (2018), [arXiv:1605.04909 \[astro-ph.CO\]](https://arxiv.org/abs/1605.04909).
- [5] E. Aprile *et al.* (XENON), First Dark Matter Search with Nuclear Recoils from the XENONnT Experiment, *Phys. Rev. Lett.* **131**, 041003 (2023), [arXiv:2303.14729 \[hep-ex\]](https://arxiv.org/abs/2303.14729).
- [6] C. A. J. O’Hare, New Definition of the Neutrino Floor for Direct Dark Matter Searches, *Phys. Rev. Lett.* **127**, 251802 (2021), [arXiv:2109.03116 \[hep-ph\]](https://arxiv.org/abs/2109.03116).
- [7] J. Billard, L. Strigari, and E. Figueroa-Feliciano, Implications of neutrino backgrounds on the reach of next generation dark matter direct detection experiments, *Phys. Rev. D* **89**, 023524 (2014), [arXiv:1307.5458 \[hep-ph\]](https://arxiv.org/abs/1307.5458).
- [8] F. Ruppin, J. Billard, E. Figueroa-Feliciano, and L. Strigari, Complementarity of dark matter detectors in light of the neutrino background, *Phys. Rev. D* **90**, 083510 (2014), [arXiv:1408.3581 \[hep-ph\]](https://arxiv.org/abs/1408.3581).
- [9] D. S. Akerib *et al.*, Snowmass2021 Cosmic Frontier Dark Matter Direct Detection to the Neutrino Fog, in *Snowmass 2021* (2022) [arXiv:2203.08084 \[hep-ex\]](https://arxiv.org/abs/2203.08084).
- [10] J. Billard *et al.*, Direct detection of dark matter—APPEC committee report*, *Rept. Prog. Phys.* **85**, 056201 (2022), [arXiv:2104.07634 \[hep-ex\]](https://arxiv.org/abs/2104.07634).
- [11] E. Aprile *et al.* (XENON), First Measurement of Solar ^8B Neutrinos via Coherent Elastic Neutrino-Nucleus Scattering with XENONnT, (2024), [arXiv:2408.02877 \[nucl-ex\]](https://arxiv.org/abs/2408.02877).
- [12] E. Aprile *et al.* (XENON1T), Conceptual design and simulation of a water Cherenkov muon veto for the XENON1T experiment, *JINST* **9**, P11006, [arXiv:1406.2374 \[astro-ph.IM\]](https://arxiv.org/abs/1406.2374).
- [13] M. Murra, D. Schulte, C. Huhmann, and C. Weinheimer, Design, construction and commissioning of a high-flow radon removal system for XENONnT, *Eur. Phys. J. C* **82**, 1104 (2022), [arXiv:2205.11492 \[physics.ins-det\]](https://arxiv.org/abs/2205.11492).
- [14] E. Aprile *et al.* (XENON), Removing krypton from xenon by cryogenic distillation to the ppq level, *Eur. Phys. J. C* **77**, 275 (2017), [arXiv:1612.04284 \[physics.ins-det\]](https://arxiv.org/abs/1612.04284).
- [15] J. Aalbers *et al.*, AxFoundation/strax: Stream analysis for xenon tpc (2024).
- [16] XENON Collaboration, XENONnT/straxen: Streaming analysis for xenon (2024).
- [17] K. Petraki and R. R. Volkas, Review of asymmetric dark matter, *Int. J. Mod. Phys. A* **28**, 1330028 (2013), [arXiv:1305.4939 \[hep-ph\]](https://arxiv.org/abs/1305.4939).
- [18] D. E. Kaplan, M. A. Luty, and K. M. Zurek, Asymmetric Dark Matter, *Phys. Rev. D* **79**, 115016 (2009), [arXiv:0901.4117 \[hep-ph\]](https://arxiv.org/abs/0901.4117).
- [19] D. N. Spergel and P. J. Steinhardt, Observational evidence for selfinteracting cold dark matter, *Phys. Rev. Lett.* **84**, 3760 (2000), [arXiv:astro-ph/9909386](https://arxiv.org/abs/astro-ph/9909386).
- [20] S. Tulin and H.-B. Yu, Dark Matter Self-interactions and Small Scale Structure, *Phys. Rept.* **730**, 1 (2018), [arXiv:1705.02358 \[hep-ph\]](https://arxiv.org/abs/1705.02358).
- [21] K. M. Zurek, Multi-Component Dark Matter, *Phys. Rev. D* **79**, 115002 (2009), [arXiv:0811.4429 \[hep-ph\]](https://arxiv.org/abs/0811.4429).
- [22] N. Fornengo, P. Panci, and M. Regis, Long-Range Forces in Direct Dark Matter Searches, *Phys. Rev. D* **84**, 115002 (2011), [arXiv:1108.4661 \[hep-ph\]](https://arxiv.org/abs/1108.4661).
- [23] J. D. Lewin and P. F. Smith, Review of mathematics, numerical factors, and corrections for dark matter experiments based on elastic nuclear recoil, *Astropart. Phys.*

* Also at INFN-Roma Tre, 00146 Roma, Italy

† Now at Department of Physics & Astronomy, Bucknell University, Lewisburg, PA, USA

‡ Also at Coimbra Polytechnic - ISEC, 3030-199 Coimbra, Portugal

§ shenyang.shi@columbia.edu

¶ yuanlq@uchicago.edu

** xenon@lngs.infn.it

[1] E. Aprile *et al.* (XENON), The XENONnT dark matter experiment, *Eur. Phys. J. C* **84**, 784 (2024), [arXiv:2402.10446 \[physics.ins-det\]](https://arxiv.org/abs/2402.10446).

[2] L. Roszkowski, E. M. Sessolo, and S. Trojanowski, WIMP dark matter candidates and searches—current status and future prospects, *Rept. Prog. Phys.* **81**, 066201 (2018), [arXiv:1707.06277 \[hep-ph\]](https://arxiv.org/abs/1707.06277).

[3] G. Jungman, M. Kamionkowski, and K. Griest, Supersymmetric dark matter, *Phys. Rept.* **267**, 195 (1996),

6, 87 (1996).

[24] J. Menendez, D. Gazit, and A. Schwenk, Spin-dependent WIMP scattering off nuclei, *Phys. Rev. D* **86**, 103511 (2012), [arXiv:1208.1094 \[astro-ph.CO\]](#).

[25] S. Chang, A. Pierce, and N. Weiner, Momentum Dependent Dark Matter Scattering, *JCAP* **01**, 006, [arXiv:0908.3192 \[hep-ph\]](#).

[26] R. Foot, Mirror dark matter: Cosmology, galaxy structure and direct detection, *Int. J. Mod. Phys. A* **29**, 1430013 (2014), [arXiv:1401.3965 \[astro-ph.CO\]](#).

[27] J. Aalbers, B. Pelssers, J. R. Angevaare, and K. D. Morå, *Jelleaalbers/wimprates*: v0.5.0 (2023).

[28] J. D. Clarke and R. Foot, Mirror dark matter will be confirmed or excluded by XENON1T, *Phys. Lett. B* **766**, 29 (2017), [arXiv:1606.09063 \[hep-ph\]](#).

[29] E. Aprile *et al.*, Low-energy Neutron Calibration of XENONnT with an YBe Source (2024), in preparation.

[30] J. I. Collar, Applications of an $^{88}\text{Y}/\text{Be}$ photo-neutron calibration source to Dark Matter and Neutrino Experiments, *Phys. Rev. Lett.* **110**, 211101 (2013), [arXiv:1303.2686 \[physics.ins-det\]](#).

[31] E. Aprile *et al.* (XENON), XENONnT WIMP Search: Signal & Background Modeling and Statistical Inference, (2024), [arXiv:2406.13638 \[physics.data-an\]](#).

[32] M. Szydagis, N. Barry, K. Kazkaz, J. Mock, D. Stolp, M. Sweany, M. Tripathi, S. Uvarov, N. Walsh, and M. Woods, NEST: a comprehensive model for scintillation yield in liquid xenon, *J. Inst.* **6**, P10002 (2011).

[33] E. Aprile *et al.*, XENONnT Analysis: Signal Reconstruction, Calibration, and Event Selection, [arXiv:2409.08778 \[physics.data-an\]](#) (2024).

[34] B. Aharmim *et al.* (SNO), Combined Analysis of all Three Phases of Solar Neutrino Data from the Sudbury Neutrino Observatory, *Phys. Rev. C* **88**, 025501 (2013), [arXiv:1109.0763 \[nucl-ex\]](#).

[35] XENON Collaboration, *XENONnT/fuse: Refactor xenonnt epix and wfsim code* (2024).

[36] E. Aprile *et al.* (XENON), Search for Coherent Elastic Scattering of Solar ^8B Neutrinos in the XENON1T Dark Matter Experiment, *Phys. Rev. Lett.* **126**, 091301 (2021), [arXiv:2012.02846 \[hep-ex\]](#).

[37] D. Baxter *et al.*, Recommended conventions for reporting results from direct dark matter searches, *Eur. Phys. J. C* **81**, 907 (2021), [arXiv:2105.00599 \[hep-ex\]](#).

[38] J. N. Bahcall, E. Lisi, D. E. Alburger, L. De Braeckeleer, S. J. Freedman, and J. Napolitano, Standard neutrino spectrum from B-8 decay, *Phys. Rev. C* **54**, 411 (1996), [arXiv:nucl-th/9601044](#).

[39] XENON Collaboration, *XENONnT/axidence: strax-based data-driven accidental coincidence background simulation and peak-level salting* (2024).

[40] C. H. Faham, V. M. Gehman, A. Currie, A. Dobi, P. Sorensen, and R. J. Gaitskell, Measurements of wavelength-dependent double photoelectron emission from single photons in VUV-sensitive photomultiplier tubes, *JINST* **10** (09), P09010, [arXiv:1506.08748 \[physics.ins-det\]](#).

[41] D. S. Akerib *et al.* (LZ), Enhancing the sensitivity of the LUX-ZEPLIN (LZ) dark matter experiment to low energy signals, (2021), [arXiv:2101.08753 \[astro-ph.IM\]](#).

[42] P. Sorensen, Anisotropic diffusion of electrons in liquid xenon with application to improving the sensitivity of direct dark matter searches, *Nucl. Instrum. Meth. A* **635**, 41 (2011), [arXiv:1102.2865 \[astro-ph.IM\]](#).

[43] E. Aprile *et al.* (XENON), Search for New Physics in Electronic Recoil Data from XENONnT, *Phys. Rev. Lett.* **129**, 161805 (2022), [arXiv:2207.11330 \[hep-ex\]](#).

[44] E. Aprile *et al.* (XENON), Light Dark Matter Search with Ionization Signals in XENON1T, *Phys. Rev. Lett.* **123**, 251801 (2019), [arXiv:1907.11485 \[hep-ex\]](#).

[45] J. Aalbers *et al.* (LZ), First Dark Matter Search Results from the LUX-ZEPLIN (LZ) Experiment, *Phys. Rev. Lett.* **131**, 041002 (2023), [arXiv:2207.03764 \[hep-ex\]](#).

[46] S. Li *et al.* (PandaX), Search for Light Dark Matter with Ionization Signals in the PandaX-4T Experiment, *Phys. Rev. Lett.* **130**, 261001 (2023), [arXiv:2212.10067 \[hep-ex\]](#).

[47] W. Ma *et al.* (PandaX), Search for Solar B8 Neutrinos in the PandaX-4T Experiment Using Neutrino-Nucleus Coherent Scattering, *Phys. Rev. Lett.* **130**, 021802 (2023), [arXiv:2207.04883 \[hep-ex\]](#).

[48] G. Angloher *et al.* (CRESST), Limits on momentum-dependent asymmetric dark matter with CRESST-II, *Phys. Rev. Lett.* **117**, 021303 (2016), [arXiv:1601.04447 \[astro-ph.CO\]](#).

[49] P. Agnes *et al.* (DarkSide), DarkSide-50 532-day Dark Matter Search with Low-Radioactivity Argon, *Phys. Rev. D* **98**, 102006 (2018), [arXiv:1802.07198 \[astro-ph.CO\]](#).

[50] E. D. Nobile, M. Kaplinghat, and H.-B. Yu, Direct detection signatures of self-interacting dark matter with a light mediator, *J. Cosmol. Astropart. Phys.* **2015** (10), 055.

[51] P. Klos, J. Menéndez, D. Gazit, and A. Schwenk, Large-scale nuclear structure calculations for spin-dependent WIMP scattering with chiral effective field theory currents, *Phys. Rev. D* **88**, 083516 (2013).

[52] G. J. Feldman and R. D. Cousins, A Unified approach to the classical statistical analysis of small signals, *Phys. Rev. D* **57**, 3873 (1998), [arXiv:physics/9711021](#).

[53] XENON Collaboration, *XENONnT/alea: A tool to perform toymc-based inference constructions* (2024).

[54] G. Cowan, K. Cranmer, E. Gross, and O. Vitells, Power-Constrained Limits, (2011), [arXiv:1105.3166 \[physics.data-an\]](#).